

# Density Matrix Renormalization Group study of superconducting pairing near the quarter-filled Wigner crystal

R. Torsten Clay\* and Beau A. Thompson

*Department of Physics & Astronomy, and HPC<sup>2</sup> Center for Computational Sciences,  
Mississippi State University, Mississippi State, MS 39762*

(Dated: today)

Charge ordering is often found in the phase diagram of unconventional superconductors in close proximity to the superconducting state. This has led to the suggestion that fluctuations of charge order can mediate superconducting pairing. While several mechanisms can lead to charge order, one common mechanism is the long-range Coulomb interaction, resulting in a Wigner crystal charge ordered state. For an electron density of 0.5 per site we investigate the extended Hubbard model on the two-dimensional square lattice using exact diagonalization and density matrix renormalization group methods. Our results show that the strength of pairing decreases with the nearest-neighbor Coulomb interaction strength  $V$  and remains weaker than the tendency of pairing for non-interacting electrons.

## I. INTRODUCTION

In strongly correlated materials broken symmetry states mediated by electron-electron (e-e) interactions are often found proximate to unconventional superconductivity (SC). Antiferromagnetic (AFM) magnetic order has been studied in the most detail because of its prominent role in the high- $T_c$  cuprates, but charge order (CO) is a second broken symmetry state found in many unconventional superconductors including the cuprates [1], organic charge-transfer solids (CTS) [2], iron-based superconductors [3], moire superlattice systems [4], and other materials [5]. As with the many proposals that AFM fluctuations can mediate SC, similar proposals have suggested that fluctuations of the CO can mediate pairing.

Charge order can take many forms depending on the lattice and carrier density of the material, and can be mediated by different mechanisms. In this paper we focus on Wigner crystal (WC) CO driven by the long-range Coulomb repulsion. The possibility of SC mediated by fluctuations of the WC has been suggested for a number of different materials with a variety of different lattice structures [6–17]. In this paper we focus on the simplest possible system giving WC CO, the extended Hubbard model on a square lattice at density 0.5 per site (quarter filling). We present exact diagonalization and Density Matrix Renormalization Group (DMRG) results for zero temperature superconducting pairing correlations near the WC state. Our results find no evidence for SC near the WC state. The paper is organized as follows: Section II defines the model and correlation functions we consider, Section III presents our numerical results, and Section IV summarizes our findings. The Appendix includes additional information on the implementation and performance of the parallel DMRG method used in this work.

## II. THEORETICAL MODEL AND COMPUTATIONAL TECHNIQUE

We consider the extended Hubbard model (EHM),

$$H = -t \sum_{\langle ij \rangle, \sigma} (c_{i,\sigma}^\dagger c_{j,\sigma} + H.c.) + U \sum_i n_{i,\uparrow} n_{i,\downarrow} + V \sum_{\langle ij \rangle} n_i n_j. \quad (1)$$

In Eq. 1,  $c_{i,\sigma}^\dagger$  creates an electron of spin  $\sigma$  on site  $i$ ;  $n_{i,\sigma} = c_{i,\sigma}^\dagger c_{i,\sigma}$  and  $n_i = n_{i,\uparrow} + n_{i,\downarrow}$ . The sites  $i$  and  $j$  in  $\langle ij \rangle$  are nearest neighbor (n.n.) sites on a square lattice. We give energies in units of  $t$ .  $U$  and  $V$  are the onsite and n.n. Coulomb interactions, respectively. We take the electron density  $\rho = 0.5$ .

For the EHM at  $\rho = 0.5$  on a square lattice with  $U$  large compared to  $t$ , the ground state is a WC CO when  $V$  exceeds a critical value  $V_c$ . At  $\rho = 0.5$ , in one dimension (1D) the pattern of CO is  $\dots 1010\dots$ , where ‘0’ (‘1’) represents a charge density  $\langle n_i \rangle = 0.5 - \delta n$  ( $0.5 + \delta n$ ); in 2D on a square lattice the CO pattern is a checkerboard with  $\mathbf{Q}_{\text{CO}} = (\pi, \pi)$ .  $V_c$  is known exactly in 1D in the limit  $U \rightarrow \infty$ , where  $V_c = 2$ . For finite  $U$ ,  $V_c$  is larger than 2 in 1D [2]. At  $U = 8$ ,  $V_c \sim 2.9$  in 1D [18] and  $V_c \sim 2.8$  for a two-leg ladder [19]. On the 2D square lattice  $V_c$  is expected to be smaller than in 1D, but is not known precisely except in the spinless fermion limit, where on the 2D square lattice  $V_c = 0.45 \pm 0.02$  [20].

There are many proposals that unconventional SC occurs in Eq. 1 within the metallic phase of the model with  $V \lesssim V_c$  [6–17]. One suggestion is that following a slave boson transformation of Eq. 1 in the large  $U$  and  $SU(N)$  large  $N$  limits, the effective bosons mediate attraction between the remaining quasiparticles [6]. Because of the strong n.n. Coulomb repulsion, pairing would be expected to involve electrons on next-nearest neighbor (n.n.n.) sites. While the theory was originally applied to a square lattice subsequent work considered triangular [21] and other lattices [16, 17]. Calculations that sup-

\* r.t.clay@msstate.edu

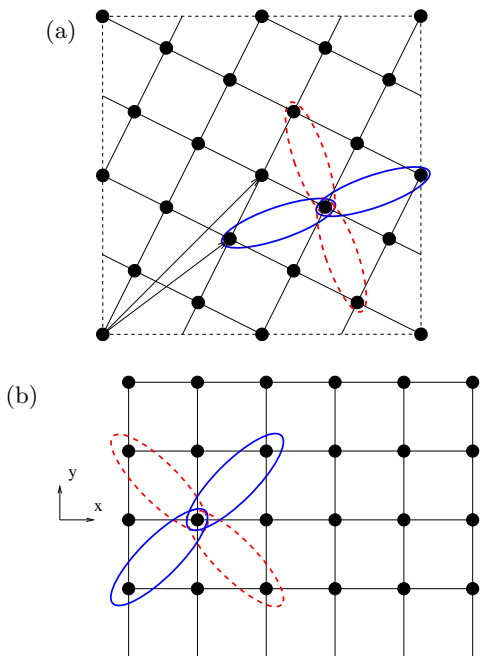


FIG. 1. (color online) (a) Periodic 20-site cluster. The arrows show the furthest and next-furthest possible distances. (b) width four cylindrical lattice. For (b) boundary conditions are periodic (open) in  $\hat{y}$  ( $\hat{x}$ ). A  $d_{xy}$  pair is shown on each figure. Solid (dashed) lines correspond to singlets with opposite sign in Eq. 5.

port the presence of SC near Wigner crystal CO include slave boson techniques [6], mean-field theory [9], random phase approximation (RPA) [10, 13, 16, 21], fluctuation exchange (FLEX) [8, 17], and variational quantum Monte Carlo (QMC) [11, 14, 15].

In our calculations we fix the value of  $U$  at 8 and consider the effect of increasing  $V$ . Correlation functions we measure as a function of  $\mathbf{r}_{ij} \equiv \mathbf{r}_i - \mathbf{r}_j$  include the charge-charge correlation  $c(\mathbf{r}_{ij})$ ,

$$c(\mathbf{r}_{ij}) = \langle (n_i - \langle n_i \rangle)(n_j - \langle n_j \rangle) \rangle, \quad (2)$$

and the spin-spin correlation  $s(\mathbf{r}_{ij})$ ,

$$s(\mathbf{r}_{ij}) = \langle (n_{i,\uparrow} - n_{i,\downarrow})(n_{j,\uparrow} - n_{j,\downarrow}) \rangle. \quad (3)$$

As an order parameter of the CO phase we calculate the charge structure factor,

$$S(\mathbf{q}) = \frac{1}{N} \sum_{ij} e^{i\mathbf{q} \cdot \mathbf{r}_{ij}} c(\mathbf{r}_{ij}), \quad (4)$$

at  $\mathbf{Q} = (\pi, \pi)$ .

We define the singlet superconducting pair creation operator as

$$\Delta_i^\dagger = \mathcal{N} \sum_v g_v (c_{i,\uparrow}^\dagger c_{i+\vec{\tau}_v,\downarrow}^\dagger - c_{i,\downarrow}^\dagger c_{i+\vec{\tau}_v,\uparrow}^\dagger), \quad (5)$$

where  $\mathcal{N}$  is a normalization factor and  $g_\nu = \pm 1$  a relative phase (see Fig. 1). The pair-pair correlation is defined

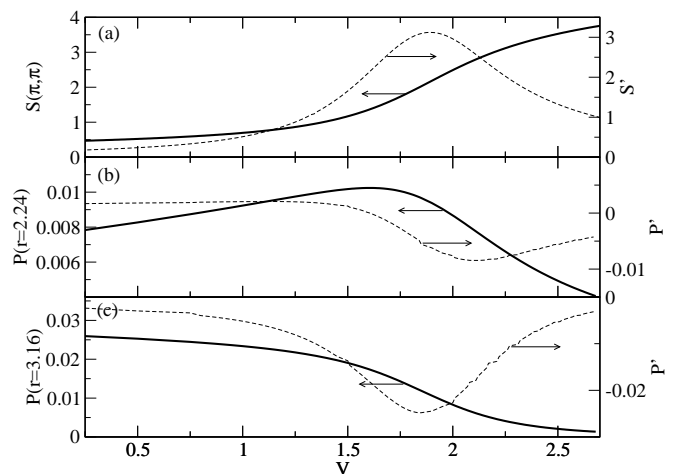


FIG. 2. Exact results for the 20 site periodic lattice of Fig. 1(a). Solid lines are the correlation functions calculated on a grid of spacing  $\Delta V = 0.01$ . Dashed lines are derivatives with respect to  $V$  calculated using a centered finite difference (see text). (a) Charge structure factor at  $\mathbf{Q} = (\pi, \pi)$  as a function of  $V$ . (b)-(c)  $d_{xy}$  pair-pair correlation function at  $r = 2.24$  and  $r = 3.16$ .

as  $P(r) = \frac{1}{2}(\langle \Delta_i^\dagger \Delta_j \rangle + \langle \Delta_i \Delta_j^\dagger \rangle)$ . For completeness we consider pairing where  $\vec{\tau}_\nu$  in Eq. 5 corresponds to both n.n. and n.n.n. sites. The most likely pairing symmetry involves a superposition of n.n.n. pairs in  $s_{xy}$  or  $d_{xy}$  form as shown in Fig. 1. In a 2D superconductor at zero temperature,  $P(r)$  must exhibit long-range order, with  $P(r)$  extrapolating to a constant for  $r \rightarrow \infty$ . We present results for two different lattices: a 20-site periodic cluster (Fig. 1(a)) which is one of the largest that can be solved exactly, and a width four cylindrical lattice of length  $L$  with periodic boundaries in the short dimension and open boundaries in the long dimension (Fig. 1(b)).

### III. RESULTS

#### A. Exact diagonalization

While the lattice sizes available to exact solution are limited, they can provide information on whether a given interaction strengthens or weakens pairing correlations [22]. In particular, the derivative of correlation functions with respect to a parameter of the Hamiltonian (here  $V$ ) can be very useful in locating quantum phase transitions [22]. In Fig. 2(a) we plot  $S(\pi, \pi)$  versus  $V$ . In the thermodynamic limit a discontinuous increase in  $S(\pi, \pi)$  is expected at  $V = V_c$ . The derivative  $S' = dS(\pi, \pi)/dV$  should then peak at  $V = V_c$ . In Fig. 2(a) we also plot  $S'$ , which peaks at  $V \approx 1.9$ , providing an estimate for  $V_c$ .

For the 20 site cluster we found that singlet  $d_{xy}$  pair-pair correlations are the dominant pairing symmetry; they are significantly stronger in magnitude than triplet pair-pair correlations as well as n.n. ( $s$  or  $d_{x^2-y^2}$ ) sin-

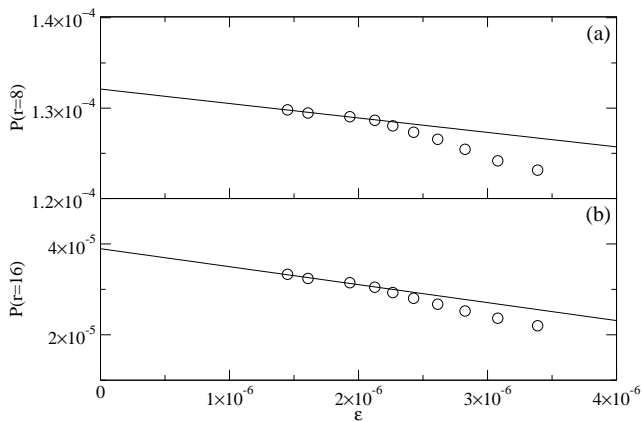


FIG. 3. The next-nearest-neighbor pair-pair correlation function  $P(r)$  for two different distances on a length  $L = 64$  cylinder (Fig. 1(b)) versus DMRG truncation error  $\epsilon$ . Here  $U = 8$ ,  $V = 1$ , and the maximum DMRG bond dimension was  $m = 20,000$ . Solid lines show a linear extrapolation using the four smallest  $\epsilon$  points.

glet correlations. In Figs. 2(b)-(c) we plot the  $d_{xy}$  pair-pair correlation as a function of  $V$  for two values of  $r$ . The values of  $r$  (see Fig. 1(a)) are chosen such that the pairs in  $P(r)$  do not contain overlapping lattice points [22]. Fig. 2(b) shows that  $P(r)$  is enhanced by  $V$  for  $r=2.24$ , with  $P(r)$  increasing with increasing  $V$  compared to its value at  $V = 0$ . However, the pair separation distance in Fig. 2(b) is the shortest possible between two non-overlapping pairs, and lattice sites comprising the pairs are within n.n. distance of each other. Correlations at the furthest possible distance ( $r=3.16$ , Fig. 2(c)) only show a continuous decrease with increasing  $V$ . In Fig. 2(b)-(c) we also plot the derivatives  $P' = dP(r)/dV$  at each distance. For a metal–superconductor–charge order sequence of phases,  $P(r)$  would increase with  $V$  and  $dP/dV$  should show a peak as in Fig. 2(a), and as  $V$  increases further, a second negative peak at the transition to the CO state. In the situation where no SC state exists and instead a metal–charge order transition occurs, mobility for both single particles as well as pairs will decrease at  $V_c$ , resulting in single a negative peak in  $dP/dV$  at  $V_c$ . We find only a negative peak in  $dP/dV$  (Figs. 2(b)-(c)), suggesting the latter situation. The minima in  $dP/dV$  is within  $\Delta V \sim \pm 0.2$  of where the maxima in  $dS/dV$  occurs, suggesting that both correspond to  $V = V_c$ . We do not see any evidence for a maxima in  $dP/dV$  preceding the minima, suggesting that no SC phase is present between the metallic and CO phases.

## B. DMRG

DMRG [23, 24] is a powerful numerical method for studying quasi-1D quantum systems because of its accuracy and unbiased nature. 2D systems are however challenging to solve in DMRG. To approach 2D, cylin-

drical lattices may be used with periodic boundaries in the transverse direction and open boundaries in the long dimension. In this approach the required DMRG bond dimension  $m$  increases exponentially with respect to the transverse dimension. Nevertheless, DMRG results on long cylinders are useful to understand the distance dependence of correlation functions.

Compared to the Hubbard and  $t$ - $J$  models, the extended Hubbard model including  $V$  has not been widely studied on 2D lattices using DMRG, except for the case of spinless fermions [20, 25]. The effect of longer-ranged Coulomb interactions has however been studied with DMRG for some time in quasi-1D systems [26, 27]. The success of the DMRG algorithm even with longer-ranged Coulomb interactions has been attributed to the finding that diagonal interactions do not increase entanglement entropy of states [27]. One disadvantage of incorporating  $V$  within DMRG is an overall slower method due to including more interactions in the Hamiltonian. Recently the effect of an attractive n.n.  $V$  interaction was studied on width four cylinders of length of up to 64 [28].

Our DMRG calculations used the ITensor library [29] and real-space parallelization [30]. We used a two-site DMRG update and particle number and  $S_z$  conservation. To ensure convergence of the results we performed many DMRG sweeps at small and intermediate bond dimension and incorporated a random “noise” to help prevent the method from becoming stuck in local minima. The maximum bond dimension we used was  $m = 21,000$ , with a minimum DMRG truncation error of  $\epsilon \sim 10^{-6}$  or less. Further details of our parallel DMRG method are given in the Appendix.

We extrapolated all observables to zero DMRG truncation error  $\epsilon$ . Fig. 3 shows typical extrapolations of the  $d_{xy}$  pair-pair correlation function at two different distances on the width four cylinder for the largest length we considered ( $L = 64$ ). In the DMRG results presented in this section, the error bars on each point are the estimated error in the linear truncation error extrapolation. In most cases this estimated error is smaller than the plotted symbol sizes. Using DMRG we calculated charge and spin correlations, pair-pair correlations for single pairs of n.n. or n.n.n. sites, and pair-pair correlations for  $s$ ,  $d_{x^2-y^2}$ ,  $s_{xy}$ , and  $d_{xy}$  symmetries. On cylindrical lattices with open boundaries, correlations of distance up to  $r_{\max} = L/2$  can be measured.

### 1. Charge and spin correlations

In open cylinders a structure factor similar to Eq. 4 can be defined [19],

$$\bar{S}(\mathbf{q}) = \frac{1}{N} \sum_{ij} e^{i\mathbf{q}\cdot\mathbf{r}_{ij}} \bar{c}(\mathbf{r}_{ij}), \quad (6)$$

where  $\bar{c}(\mathbf{r}_{ij})$  is the charge-charge correlation averaged over  $N_{\text{av}}$  equivalent  $(i, j)$  pairs to reduce the effect of

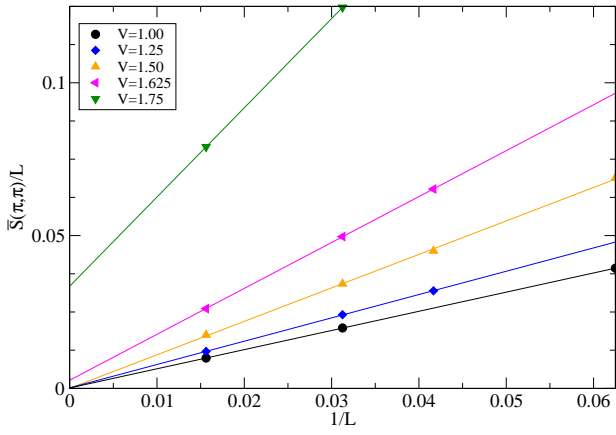


FIG. 4. (color online) Finite-size scaling of the charge structure factor for different  $V$  and lattice lengths  $L$ . DMRG extrapolation errors are smaller than the symbol sizes; lines are fits to the points.

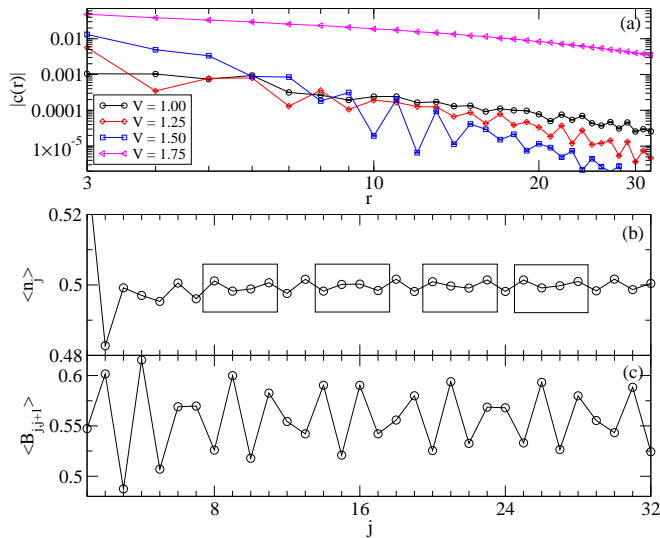


FIG. 5. (color online) (a) Charge-charge correlation function for the  $L = 64$  lattice. (b) Charge density for the  $L = 64$  lattice with  $V = 1.50$ . Boxes indicate local regions of competing charge order. (c) Bond orders.

open boundaries:

$$\bar{c}(\mathbf{r}_{ij}) = \frac{1}{N_{\text{av}}} \sum_{(i,j)} c(\mathbf{r}_{ij}). \quad (7)$$

As in Reference [19], we take  $N_{\text{av}} = 6$ . In the CO phase  $\bar{S}(\pi, \pi)/L$  should extrapolate to a finite value for  $L \rightarrow \infty$ . Fig. 4 shows the finite-size scaling of  $\bar{S}(\pi, \pi)/L$ , demonstrating that  $V_c$  is in the range  $1.50 < V_c < 1.625$ . In Fig. 5(a) we plot  $c(\mathbf{r}_{ij})$ , where  $i$  is a site on the 4th column of the lattice and  $j$  a site on the same row. The large increase in  $c(r)$  between  $V = 1.50$  and  $V = 1.75$  is consistent with the structure factor results of Fig. 4. More puzzling is the behavior of the long-range charge correlations in Fig. 5(a). For

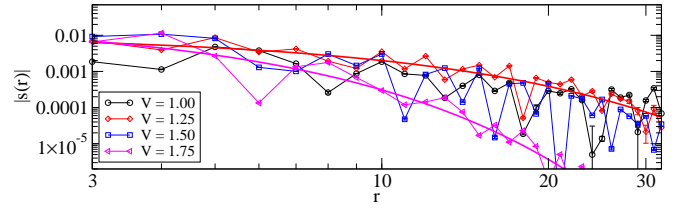


FIG. 6. (color online) Spin-spin correlation function for the  $L = 64$  lattice. Lines are fits to an exponential function (see text).

$r \lesssim 9$   $c(r)$  increases in magnitude with increasing  $V$ , but the long-distance  $c(r)$  decreases in magnitude with increasing  $V$  until  $V$  exceeds  $V_c$ . We checked carefully that this result is not a numerical artifact by using different DMRG starting states and by applying a pinning field to bias the system to uniform charge order. We also verified the effect in both  $L = 64$  and shorter length lattices.

The decrease in long-range charge correlation despite the increase of  $V$  can be understood by examining (see Fig. 5(b)-(c)) the charge density  $\langle n_j \rangle$  and bond order  $\langle B_{j,j+1} \rangle$ , where  $B_{j,j+1} = \sum_{\sigma} (c_{j,\sigma}^{\dagger} c_{j+1,\sigma} + H.c.)$ . In  $B_{j,j+1}$  we choose sites  $j$  and  $j+1$  as n.n. sites along the  $x$  axis. In Fig. 5(b) and (c) only half of the lattice is shown, as the other half is identical due to mirror plane symmetry. At carrier density  $\rho=0.5$  charge, spin, and bond degrees of freedom are strongly coupled, and electron-phonon (e-p) as well as e-e interactions both play important roles [2]. In lattices with open boundary conditions, away from the lattice edges charge densities and bond orders take on the same pattern found in a Hamiltonian including *both* e-e and e-p interactions, in the limit of  $0^+$  e-p coupling strength [31]. In 1D for  $\rho=0.5$  with finite  $U$  but  $V < V_c$ , two density-wave states are found [32]: first, a  $4k_F$  bond order wave (BOW) state with uniform charge density and alternating strong-weak bond orders, and second a  $2k_F$  (period 4) charge ordered state. These states compete with the WC CO.

As shown in Fig. 5(b) and (c), for  $V \lesssim V_c$  we find regions of the  $4k_F$  BOW/ $2k_F$  CO state (inside the boxes in Fig. 5(b)), interspersed with regions of  $\dots 1010 \dots$  CO favored by large  $V$  (found in between the boxes in Fig. 5(b)). This shows that in real systems with a finite e-p coupling, the phase immediately adjacent to the  $\dots 1010 \dots$  CO would not be metallic, but rather  $4k_F$  bond distorted, with possibly coexisting  $2k_F$  charge order. which we comment further on in Section IV.

In the CO state, AFM order is expected to coexist with the CO [2]. On a square lattice the periodicity of the AFM order would be  $\mathbf{Q}_{\text{AFM}} = (\pi, 0), (0, \pi)$ . Fig. 6 shows the spin-spin correlations as a function of increasing  $V$ . For  $V > V_c$  we do see the expected  $(\pi, 0), (0, \pi)$  spin order in the short range, but spin correlations decay exponentially with distance, indicating the presence of a spin gap. In the CO state on the width 4 cylinder, the sites with large charge density form an effective diagonal spin ladder (see Fig. 4 of Reference 33), which in

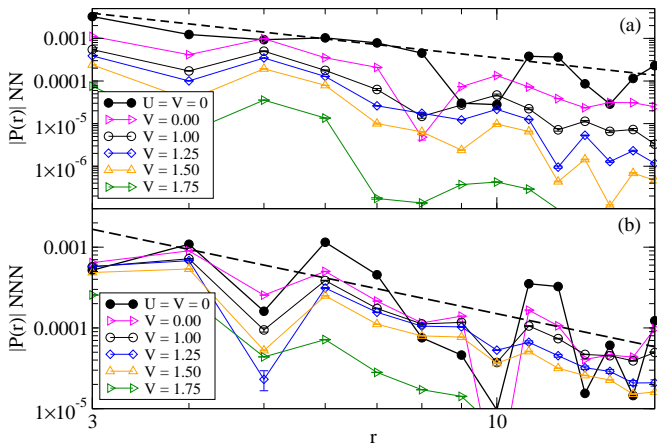


FIG. 7. (color online) (a) nearest-neighbor and (b) next-nearest-neighbor pair-pair correlations versus distance for the  $L = 32$  cylinder. The dashed lines are the power law  $r^{-2}$ .

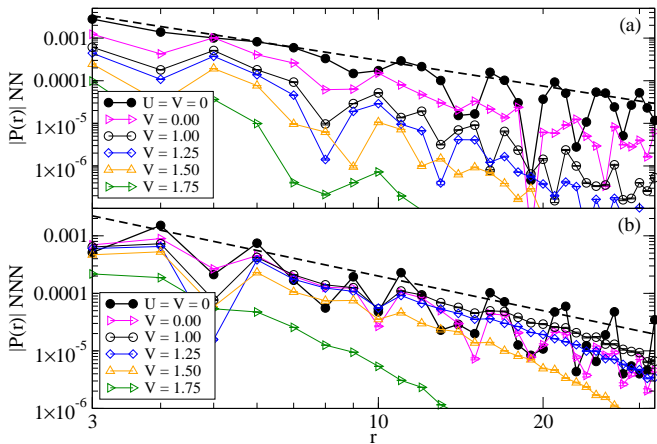


FIG. 8. (color online) (a) nearest-neighbor and (b) next-nearest-neighbor pair-pair correlations versus distance for the  $L = 64$  cylinder. The dashed lines are the power law  $r^{-2}$ .

the limit of complete CO would be expected to have a spin gap, with spin correlations decaying exponentially with distance ( $\propto e^{-r/\xi}$ ). This is one difference in the open cylinders studied here compared to a fully 2D lattice, where instead long-range AFM order would coexist with CO. From a fit to the spin-spin correlations (see Fig. 6) we estimate  $\xi \sim 2.3$  at  $V = 1.75$ . For  $V < V_c$  the situation is less clear. Here, we find that the spin-spin correlations are fit slightly better by an exponential than a power law, with for example at  $V = 1.25$  a correlation coefficient of 0.89 (exponential fit with  $\xi \sim 6$ ) versus 0.86 (power law fit). An exponential decay for  $V < V_c$  could reflect a small spin gap coexisting with  $2 k_F$  CO [18], but confirming this would likely require lattices with a larger transverse widths.

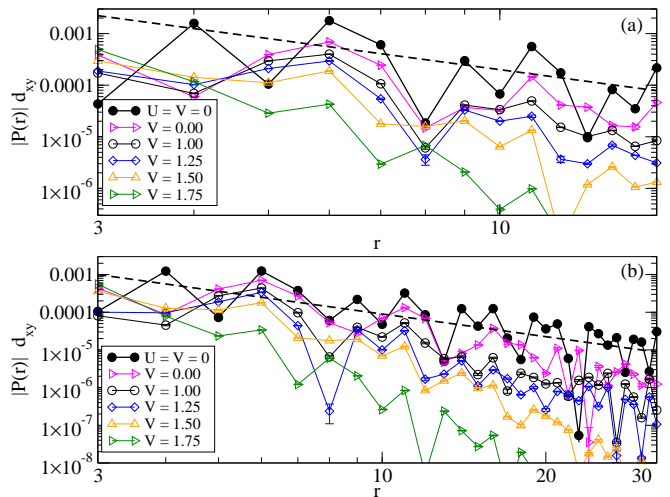


FIG. 9. (color online) (a)  $d_{xy}$  pair-pair correlations versus distance for the  $L = 32$  cylinder. (b)  $d_{xy}$  pair-pair correlations for  $L = 64$ . The dashed lines are the power law  $r^{-2}$ .

## 2. Pairing correlations

We investigated superconducting pair-pair correlation functions as a function of  $V$ ,  $r$ , and lattice size both for the correlation between individual singlet pairs, and also for  $d_{xy}$  correlations. Fig. 7(a) shows the correlation of singlet n.n. pairs along the  $x$  axis ( $\vec{r}_\nu = \hat{x}$  in Eq. 5) for an  $L=32$  lattice. To avoid end effects we measure pairing correlations from a pair located on the 5th/6th lattice columns. Because some correlations are negative we plot  $|P(r)|$ .  $P(r)$  for n.n. pairs decreases rapidly with increasing  $V$ , with a larger decrease upon entering the CO phase at  $V = 1.75$ . This is to be expected with the  $V$  interaction, which suppresses n.n. configurations in the wavefunction. Fig. 7(b) shows  $P(r)$  versus distance for n.n.n. singlet pairs ( $\vec{r}_\nu = \hat{x} + \hat{y}$ ). The n.n.n. pairing correlation also monotonically decreases in strength with increasing  $V$ , a trend that is clearest in the long-range points ( $10 \leq r \leq 20$  on Fig. 7(b)) for  $V > 1$ . Note that the apparent increase at  $r = 5$  for  $V = 1.5$  in Fig. 7(b) is due to taking the absolute value of a negative correlation. Fig. 8 shows n.n. and n.n.n. pair-pair correlations for a longer  $L = 64$  cylinder. One difference for  $L = 64$  is that long range n.n.n. correlations are slightly weaker at  $V = 0$  compared to  $V = 1$ , but like  $L = 32$  decrease in strength with larger  $V$ . The filled circles in Fig. 7-8 show  $P(r)$  for the uncorrelated ( $U = V = 0$ ) system.  $P(r)$  for the interacting systems is clearly weaker.

Because pairing correlations based on only single pairs may not distinguish between  $d$ -wave and “plaquette” pairing [34], we also calculated  $P(r)$  for full  $s$ ,  $d_{x^2-y^2}$ ,  $s_{xy}$ , and  $d_{xy}$  pairing symmetries. We found that pair-pair correlations for  $s$ ,  $d_{x^2-y^2}$ , and  $s_{xy}$  pair symmetries were weaker than  $d_{xy}$  pairing, and show here only results for  $d_{xy}$  pair-pair correlations. Fig. 9(a) shows the  $r$  and  $V$  dependence of  $P(r)$  for  $d_{xy}$  pairing on the  $L = 32$

cylinder. At very short distances ( $r = 3$ ) the  $d_{xy}$  pair-pair correlation is noticeably stronger in the interacting system. However, again at large  $r$ , we find a nearly continuous decrease of  $P(r)$  with increasing  $V$ . In Fig. 9(b) we show  $P(r)$  for  $L = 64$ , which also clearly shows that  $P(r)$  decreases with increasing  $V$  at long range.

The pairing correlations we measure appear to decay as power laws for  $V < V_c$ . In a quasi-1D system of Luther-Emery type with dominant pairing correlations such as the doped two-leg Hubbard ladder, pair-pair correlations would however decay slower than  $r^{-1}$  [35]. One can also argue that if pairing correlations decay slower than  $r^{-2}$  in 2D, this will lead to a diverging susceptibility and SC [36]. In all cases, we find decay faster than  $r^{-2}$  (see dashed lines in Figs.7-9) strongly suggesting that SC is absent in this model.

#### IV. DISCUSSION AND CONCLUSIONS

We have presented charge, bond, spin, and pairing correlations for the  $\rho = 0.5$  extended Hubbard model on the square lattice. We expect that on wider cylinders  $V_c$  will be smaller than the  $V_c \sim 1.500-1.625$  we find here, as is found in the spinless  $t$ - $V$  model [20]. Another difference between the cylinders accessible to DMRG versus an isotropic 2D lattice is that the ground state for  $V > V_c$  is spin gapped, with spin correlations decaying quickly with distance as opposed to the long-range AFM order found in 2D.

We find that long-range charge correlations become weaker with increasing  $V$ . This result has important implications for real  $\rho = 0.5$  materials in the presence of e-p interactions, especially the organic CTS [2]. In this case, the ground state in the  $V < V_c$  region will likely not be metallic, but will instead have another type of broken symmetry. Calculations including both e-e and e-p interactions on a  $4 \times 4$  lattice previously found transitions between the Wigner crystal CO and other charge/bond/spin broken symmetry states as a function of  $V$  [37]. The broken symmetry state found for  $V < V_c$  depends on several factors, principally the degree of lattice frustration [37, 38]. For weak lattice frustration the  $V < V_c$  state will have dimer-based AFM order [37, 38]. For stronger frustration, a charge-ordered Paired Electron Crystal (PEC) occurs, with  $2k_F$  charge order following the pattern  $\dots 0110\dots$  [37, 38]. The spin-gapped PEC state combines valence-bond and charge order. As  $V$  increases, Fig. 5 shows that regions of WC CO would break up the bond-ordered state, with the WC CO regions likely growing in size with  $V$  until long-range CO is reached at  $V = V_c$ . Further DMRG calculations on frustrated lattices will be of interest.

Our most important result is that we find no evidence for a charge-fluctuation mediated superconducting state proximate to the WC CO state in the EHM. With increasing  $V$ , superconducting pair-pair correlations continuously become weaker in magnitude for pair separa-

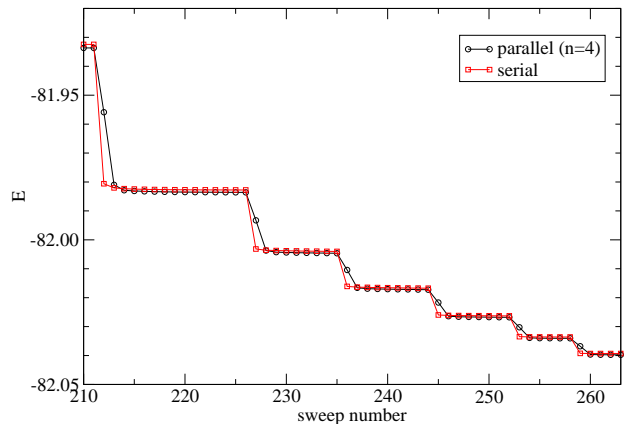


FIG. 10. (color online) Energy versus sweep number for the serial code (squares) and the real-space parallel DMRG using 4 processors. The system was the  $L = 32$  cylinder with  $U = 8$  and  $V = 1$ . From left to right, sweeps used a bond dimension of 3200, 4800, 6000, 7000, 8000, 9000, and 10000.

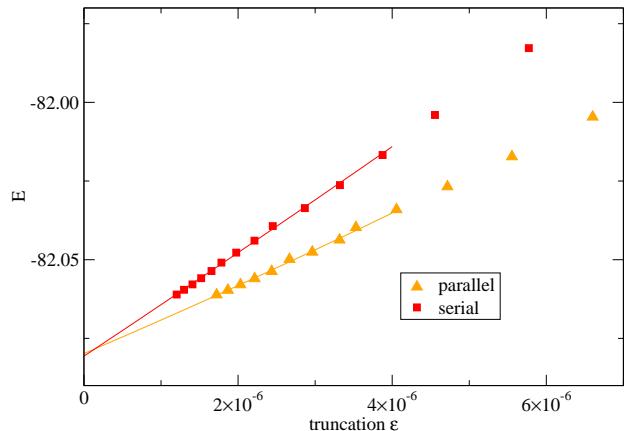


FIG. 11. (color online) Energy versus DMRG truncation error using serial DMRG (squares) the parallel algorithm with four processors (triangles). System size and parameters were the same as Fig. 10. Lines are quadratic fits using the points with  $\epsilon < 4 \times 10^{-6}$ .

tions beyond a few lattice spacings. From comparing  $L = 64$  to  $L = 32$ , we do not see any signs that pairing correlations will become dominant on longer lattices. Furthermore, long-range pair-pair correlations in the region near the CO state are always weaker than pair-pair correlations of uncorrelated particles.

#### ACKNOWLEDGMENTS

This work was supported by the National Science Foundation grant number DMR-1950208.

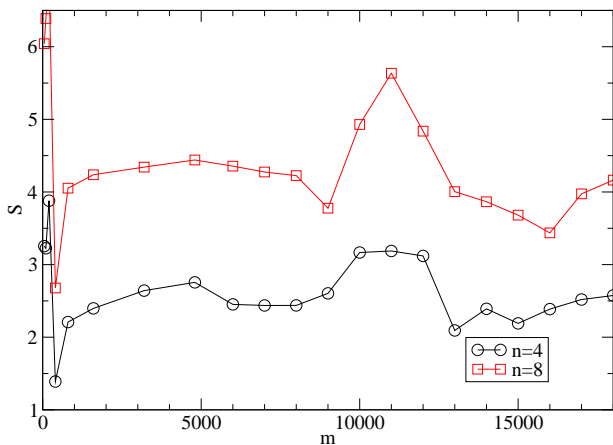


FIG. 12. (color online) Effective parallel speedup  $S$  (see text) versus DMRG bond dimension  $m$ . Circles (squares) are for 4 (8) parallel processors. System size and parameters were the same as Fig. 10.

### Appendix: Real space parallel DMRG

In this work we used the real-space parallel DMRG algorithm presented in Reference [30]. This appendix gives further details of our implementation of the method and its performance.

In this method, matrix-product tensors for the system are distributed across several parallel processors, partitioning the lattice into segments of consecutively numbered sites on each parallel process. One advantage of this over serial DMRG is that less memory is required on each parallel processor. Each parallel processor performs DMRG sweeps independently on its own lattice sites, but must perform communications with neighboring processors in order to update the shared bond between the partitions. Because of this, the overall convergence of the method is somewhat slower when compared to serial DMRG [30]. In our calculations we divided the lattice in up to  $N = 8$  segments. Each segment was assigned to one node of a parallel cluster. Each node had two Intel Xeon 6148 processors with 20 cores per processor, and 100 Gbit/s interconnects between nodes. For small  $m$  it was usually most efficient to assign multiple segments to one node. We also used OpenMP-based parallelization of linear algebra within each node.

Fig. 10 compares the energy computed using  $N = 4$  parallel processes with serial DMRG. As expected, the convergence of the energy versus the number of sweeps for the parallel DMRG is slightly slower. In practice, we find that 20-30% more DMRG sweeps are required using

the parallel algorithm, but the increased number is offset by the increase in speed.

Fig. 11 compares the energy versus truncation error for serial and parallel codes. Because of the difference in the parallel representation of the DMRG matrix product state [30], the truncation error for a given energy is slightly different between the serial and parallel codes. However, we found after extrapolation to zero truncation error, results from the serial and parallel codes agreed closely with each other. Fig. 12 shows the effective parallel speedup  $S = t_s/t_p$ , where  $t_s$  is the time per sweep of the serial code, and  $t_p$  the time per sweep of the parallel code. The serial code in this test was run on one node of 40 cores using OpenMP parallelization within each lattice partition. All parallel runs used nodes with 192 GB of memory. The serial code was run on 192 GB memory nodes for  $m < 12000$ , and 384 GB of memory nodes for  $m > 12000$ . The serial code ran more efficiently on the large-memory nodes, which accounts for the decrease in  $S$  at  $m = 13000$ . Another factor effecting the speedup was the communications latency between nodes. While Fig. 12 uses a fixed number of nodes for the parallel calculation, we found that it was usually most efficient to use the smallest number of nodes possible, to avoid the slower inter- versus intra-node communications latency. In DMRG on lattices with open boundary conditions, the quantum entanglement is reduced for lattice sites at the boundaries. Because of this, one parameter that must be tuned by hand to achieve the best performance is the size of the lattice segments on each parallel process, which can be larger for the segments at the open boundaries of the lattice.

Measuring non-local observables such as the pair-pair correlation function requires computing tensor contractions across the entire lattice. The amount of inter-processor communications to do this in parallel would be prohibitive, so such measurements must be performed on a single processor. After performing the DMRG sweeps in parallel we construct a single-processor copy of the full wavefunction by contracting the wavefunction tensors from each node, along with the connecting tensors (denoted  $V_i$  in Reference 30). Measurements of non-local correlations are then performed on a single processor. Because measuring correlations takes much less memory than performing DMRG sweeps, measurements can still be performed on a single node even when there is insufficient memory to perform the full DMRG calculation in serial. In practice multiple processors can also be used to measure different observables simultaneously to speed up the measurement process.

[1] A. Frano, S. Bianco-Canosa, B. Keimer, and R. J. Birgeneau, Charge ordering in superconducting copper oxides, *J. Phys.: Condens. Matter* **32**, 374005 (2020).

[2] R. T. Clay and S. Mazumdar, From charge- and spin-ordering to superconductivity in the organic charge-transfer solids, *Physics Reports* **788**, 1 (2019).

- [3] E. Dagotto, Colloquium: the unexpected properties of alkali metal iron selenide superconductors, *Rev. Mod. Phys.* **85**, 849 (2013).
- [4] E. C. Regan *et al.*, Mott and generalized Wigner crystal states in  $\text{WSe}_2/\text{WS}_2$  moiré superlattices, *Nature* **579**, 359 (2020).
- [5] T. Neupert, M. M. Denner, J.-X. Yin, R. Thomale, and M. Z. Hasan, Charge order and superconductivity in kagome materials, *Nat. Phys.* **18**, 137 (2022).
- [6] J. Merino and R. H. McKenzie, Superconductivity mediated by charge fluctuations in layered molecular crystals, *Phys. Rev. Lett.* **87**, 237002 (2001).
- [7] A. Greco, J. Merino, A. Foussats, and R. H. McKenzie, Spin exchange and superconductivity in a  $t$ - $J'$ - $V$  model for two dimensional quarter-filled systems, *Phys. Rev. B* **71**, 144502 (2005).
- [8] S. Onari, R. Arita, K. Kuroki, and H. Aoki, Superconductivity from long-range interaction: A crossover between the electron gas and the lattice model, *Phys. Rev. B* **73**, 014526 (2006).
- [9] S. Morohoshi and Y. Fukumoto, Superconductivity in the three-fold charge-ordered metal of the triangular-lattice extended Hubbard model, *J. Phys. Soc. Jpn.* **77**, 023708 (2008).
- [10] K. Kuroki, The origin of the charge ordering and its relevance to superconductivity in  $\theta$ -(BEDT-TTF) $_2$ X: The effect of the Fermi surface nesting and the distant electron-electron interactions, *J. Phys. Soc. Jpn.* **75**, 114716 (2006).
- [11] H. Watanabe and M. Ogata, Novel charge order and superconductivity in two-dimensional frustrated lattice at quarter filling, *J. Phys. Soc. Jpn.* **75**, 063702 (2006).
- [12] Y. Tanaka and M. Ogata, Superconductivity in  $\text{Na}_x\text{CoO}_2\cdot y\text{H}_2\text{O}$  due to charge fluctuation, *J. Phys. Soc. Jpn.* **73**, 319 (2004).
- [13] Y. Nonoyama, Y. Maekawa, A. Kobayashi, Y. Suzumura, and H. Ito, Mechanism of superconductivity in quasi-two-dimensional organic conductor  $\beta$ -(BDA-TTP) salts, *J. Phys. Soc. Jpn.* **77**, 094703 (2008).
- [14] H. Watanabe, H. Seo, and S. Yunoki, Phase competition and superconductivity in  $\kappa$ -(BEDT-TTF) $_2$ X: Importance of intermolecular Coulomb interactions, *J. Phys. Soc. Jpn.* **86**, 033703 (2017).
- [15] H. Watanabe, H. Seo, and S. Yunoki, Mechanism of superconductivity and electron-hole doping asymmetry in  $\kappa$ -type molecular conductors, *Nature Comm.* **10**, 3167 (2019).
- [16] S. Zhou, G. Kotliar, and Z. Wang, Extended Hubbard model of superconductivity driven by charge fluctuations in iron pnictides, *Phys. Rev. B* **84**, 140505(R) (2011).
- [17] Z.-J. Yao, J.-X. Li, and Z. D. Wang, Extended Hubbard model of superconductivity and charge-density-waves in the layered 2H transition metal dichalcogenides, *Phys. Rev. B* **74**, 212507 (2006).
- [18] R. T. Clay, A. B. Ward, N. Gomes, and S. Mazumdar, Bond patterns and charge-order amplitude in quarter-filled charge-transfer solids, *Phys. Rev. B* **95**, 125114 (2017).
- [19] M. Vojta, A. Hubsch, and R. M. Noack, Phase diagram of the quarter-filled extended Hubbard model on a two-leg ladder, *Phys. Rev. B* **63**, 045105 (2001).
- [20] J. P. Song and R. Clay, Monte Carlo simulations of two-dimensional fermion systems with string-bond states, *Phys. Rev. B* **89**, 075101 (2014).
- [21] Y. Tanaka, Y. Yanase, and M. Ogata, Superconductivity due to charge fluctuation in  $\theta$ -type organic conductors, *J. Phys. Soc. Jpn.* **73**, 2053 (2004).
- [22] R. T. Clay, H. Li, and S. Mazumdar, Absence of superconductivity in the half-filled band Hubbard model on the anisotropic triangular lattice, *Phys. Rev. Lett.* **101**, 166403 (2008).
- [23] S. R. White, Density matrix formulation for quantum renormalization groups, *Phys. Rev. Lett.* **69**, 2863 (1992).
- [24] U. Schollwöck, The density-matrix renormalization group, *Rev. Mod. Phys.* **77**, 259 (2005).
- [25] J. Motruk, M. P. Zaletel, R. S. K. Mong, and F. Pollman, Density matrix renormalization group on a cylinder in mixed real and momentum space, *Phys. Rev. B* **93**, 155139 (2016).
- [26] Y. Anusooya, S. K. Pati, and S. Ramasesha, Symmetrized density matrix renormalization group studies of the properties of low-lying states of the poly-para-phenylene system, *J. Chem. Phys.* **106**, 10230 (1997).
- [27] S. Sahoo, V. M. L. D. P. Goli, and S. R. ans D. Sen, Exact entanglement studies of strongly correlated systems: role of long-range interactions and symmetries of the system, *J. Phys.: Condens. Matter* **24**, 115601 (2012).
- [28] C. Peng, Y. Wang, J. Wen, Y. S. Lee, T. P. Devereaux, and H.-C. Jiang, Enhanced superconductivity by near-neighbor attraction in the doped extended Hubbard model, *Phys. Rev. B* **107**, L201102 (2023).
- [29] M. Fishman, S. R. White, and E. M. Stoudenmire, The ITensor software library for tensor network calculations, *SciPostPhys. Codebases* **4** (2022).
- [30] E. M. Stoudenmire and S. R. White, Real-space parallel density matrix renormalization group, *Phys. Rev. B* **87**, 155137 (2013).
- [31] S. Mazumdar, R. T. Clay, and D. K. Campbell, Bond-order and charge-density waves in the isotropic interacting two-dimensional quarter-filled band and the insulating state proximate to organic superconductivity, *Phys. Rev. B* **62**, 13400 (2000).
- [32] K. C. Ung, S. Mazumdar, and D. Toussaint, Metal-insulator and insulator-insulator transitions in the quarter-filled band organic conductors, *Phys. Rev. Lett.* **73**, 2603 (1994).
- [33] E. H. Kim, G. Fáth, J. Sólyom, and D. J. Scalapino, Phase transitions between topologically distinct gapped phases in isotropic spin ladders, *Phys. Rev. B* **62**, 14965 (2000).
- [34] C.-M. Chung, M. Qin, S. Zhang, U. Schollwöck, and S. R. White, Plaquette versus ordinary  $d$ -wave pairing in the  $t'$ -Hubbard model on a width-4 cylinder, *Phys. Rev. B* **102**, 041106(R) (2020).
- [35] M. Dolfi, B. Bauer, S. Keller, and M. Troyer, Pair correlations in doped Hubbard ladders, *Phys. Rev. B* **92**, 195139 (2015).
- [36] D. P. Arovas, E. Berg, S. A. Kivelson, and S. Raghu, The Hubbard model, *Annu. Rev. Condens. Matter Phys* **13**, 239 (2022).
- [37] S. Dayal, R. T. Clay, H. Li, and S. Mazumdar, Paired electron crystal: Order from frustration in the quarter-filled band, *Phys. Rev. B* **83**, 245106 (2011).
- [38] H. Li, R. T. Clay, and S. Mazumdar, The paired-electron crystal in the two-dimensional frustrated quarter-filled band, *J. Phys.: Condens. Matter* **22**, 272201 (2010).